In-situ nanoscopy of single-grain nano-morphology and ultrafast carrier dynamics in metal halide perovskites

M. Zizlsperger[1], S. Nerreter[1], Q. Yuan[2], K. B. Lohmann[2], F. Sandner[1], F. Schiegl[1], C. Meineke[1], Y. A. Gerasimenko[1], L.M. Herz[2], T. Siday[1,2,*], M. A. Huber[1,*], M. B. Johnston[2,*], R. Huber[1]

[1]*Department of Physics and Regensburg Center for Ultrafast Nanoscopy (RUN), University of Regensburg, 93040 Regensburg, Germany*

[2]*Department of Physics, University of Oxford, Clarendon Laboratory, Parks Road, Oxford, OX1 3PU, UK*

Designing next-generation light harvesting devices requires a detailed understanding of the transport of photoexcited charge carriers. The record-breaking efficiencies of metal halide perovskite solar cells have been linked to effective charge-carrier diffusion, yet the exact nature of the out-of-plane transport has remained notoriously difficult to reveal. The characteristic spatial inhomogeneity of perovskite films with nanograins and crystallographic disorder calls for a hitherto elusive in-situ resolution of the chemical composition, the structural phase, and the ultrafast dynamics of the local out-of-plane transport, all at once. Here, by pushing depth-sensitive terahertz near-field nano-spectroscopy to extreme subcycle time scales, we simultaneously probe the intrinsic out-of-plane charge-carrier diffusion and the nanoscale morphology. In films of the organic-inorganic metal halide perovskite $FA_{0.83}Cs_{0.17}Pb(I_{1-x}Cl_x)_3$ domains of the cubic α-phase are clearly distinguished from the trigonal δ-phase and PbI_2 nano-islands. By analysing deep-subcycle time shifts of the scattered terahertz waveform after photoexcitation, we access the vertical charge-carrier dynamics within single grains. On all measured locations, despite topographic irregularities, diffusion is surprisingly homogeneous on the 100-nm scale, but varies between mesoscopic regions. Linking in-situ carrier transport with nanoscale morphology and chemical composition could introduce a paradigm shift for the analysis and optimisation of next-generation optoelectronics based on nanocrystalline materials.

The rise of metal halide perovskites has prompted a revolution in optoelectronics research[1–11]. While the implementation of efficient light-emitting diodes[11,12], ultrasensitive photodetectors[13] and sub-micron-scale lasers[14,15] has showcased the versatility of the material class, its main applications are in solar cell technology. Even single-junction solar cells have reached power conversion efficiencies exceeding 26% (ref. 16). Efficient electron transport in the out-of-plane direction by diffusion plays a central role in all these applications and is thus key to unlocking the full potential of metal halide perovskites. Yet, the microscopic mechanisms are complex, owing to the presence of characteristic nanometre-sized grains and grain boundaries[17]. The understanding of the interplay of material morphology and charge-carrier diffusion is further obscured by the coexistence of different crystallographic phases at room temperature[18,19] featuring inhomogeneities even down to the atomic scale[20], whose impact on charge-carrier dynamics is largely unknown.

To access carrier diffusion, optical far-field techniques such as photoluminescence experiments[4], terahertz[6] and transient absorption spectroscopy[21] have been employed, which typically provide information on the in-plane carrier dynamics. Recently, photoluminescence[22] and transient reflectance spectroscopy[23] have been employed to gain insights into out-of-plane diffusion utilising the effect of photon reabsorption. Yet, to study the impact of nanoscale inhomogeneities and non-equilibrium dynamics such as hot-carrier effects[24] on diffusion, access to the nanoscale chemical composition, crystallographic phase, and topography should be combined with ultrafast temporal resolution. Ideally, such ultrafast videography should then track the transport of all charge carriers in the relevant out-of-plane direction, independently of optical selection rules.

Here, we advance ultrafast near-field microscopy[25–30] at terahertz (THz) frequencies[31–35] to extract the nanoscale chemical composition, crystallographic structure, and topography of metal halide perovskite films while simultaneously tracking the local out-of-plane diffusion of charge carriers on ultrafast time scales. Our depth-sensitive technique is based on a novel concept: mapping the subcycle timing of scattered THz waveforms with few-femtosecond temporal precision onto the spatiotemporal information of the charge-carrier density profile after photoexcitation. The results reveal a surprising resilience of carrier diffusion to nanoscale chemical and structural inhomogeneities.

Nanoscale chemical and crystallographic identification

We investigate a prototypical state-of-the-art vapour-deposited $FA_{0.83}Cs_{0.17}Pb(I_{1-x}Cl_x)_3$ thin film (Methods), which hosts coexisting crystallographic phases at room temperature[18,36]. Because these materials feature phase-specific phonons in the THz frequency range[37], THz time-domain spectroscopy offers an elegant way of distinguishing different crystallographic phases of the material by phonon fingerprinting; simultaneously THz radiation can couple to the Drude response of photoexcited charge carriers. Yet diffraction limits the spatial resolution of far-field THz spectroscopy to length scales more than three orders of magnitude above the typical size of crystallites. Therefore, we resort to near-field microscopy, where THz pulses are coupled into evanescent near fields at the apex of the metallic tip of an atomic force microscope[31,38] (Fig. 1a). The confined near fields interact with the sample in an area set by the tip's radius of curvature yielding a spatial resolution of ~40 nm (ref. 31). The information on the interaction is imprinted onto the scattered THz field. By electro-optically sampling[25] the complete waveform, we retrieve the full complex-valued nanoscale dielectric response[39,40] of the investigated sample. For background suppression, the scattered signal is demodulated at the j^{th} harmonic of the tip tapping frequency (Methods).

In a first step, we explore the equilibrium (unilluminated) nano-morphology of the $FA_{0.83}Cs_{0.17}Pb(I_{1-x}Cl_x)_3$ film. The topography of a representative region obtained by atomic force microscopy (Fig. 1b) shows characteristic grains with lateral dimensions on the order of 100 nm; a different region on the sample (Fig. 1b, inset) exhibits a larger 60-nm protrusion. To directly determine the chemical composition and crystallographic phase of these topographic features, we record the local THz response. We start by tracing the peak scattered signal demodulated at the second harmonic of the tip tapping frequency $\hat{E}_2$ while raster-scanning the tip across the sample. The resulting map (Fig. 1c) reveals clear correlations between scattered field and topography, where grains (grain boundaries) show an overall weaker (stronger) response. Whereas artificial signal enhancement can occur in topographic troughs[41], scattering contrast also occurs between different topographically similar flat grains (see areas around open blue spheres and orange sphere in Fig. 1b).

79 The origin of these variations can be clarified by nano-spectroscopy. We record the electric field wave-
80 form E_2 as a function of the electro-optic sampling (EOS) time t_{eos} (Fig. 1d) at three representative
81 locations (Fig. 1b, full spheres; see Extended Data Fig. 1 for unnormalized data and retraction curves).
82 Whereas the temporal shape of the main cycle of the scattered THz pulse is nearly identical for all
83 locations, differences manifest in the trailing oscillations (Fig. 1d, violet shading), which may be caused
84 by characteristic lattice vibrations. The local variations of the scattered waveform, thus, provide first
85 indications of inhomogeneities in the phonon landscape, which can be clearly seen in the spectral
86 amplitude and phase (Fig. 1e). To normalise the response for the input spectrum and eliminate artifacts
87 from indirect far-field tip illumination or tip reflections, we consider the relative spectral amplitude
88 $\tilde{E}_3/\tilde{E}_2$ (Fig. 1e, top row) and phase $\phi_3 - \phi_2$ (Fig. 1e, second row) of the third and second demodulation
89 order for the three locations (Methods).

90 The response at the first location (Fig. 1e, left column, blue spheres) is characterised by a dispersive
91 feature at 1 THz in both relative amplitude and phase. While the relative amplitude increases for high
92 frequencies, a decrease is observed in the phase. For the second spot (Fig. 1e, central column, orange
93 spheres), a broader dispersive feature is obtained in $\tilde{E}_3/\tilde{E}_2$ at 1.8 THz, accompanied by a monotonically
94 decreasing spectral phase. Finally, the response retrieved at the third spot (Fig. 1e, right column, green
95 spheres) lacks any distinct features, merely showing a monotonic increase (decrease) in the spectral
96 amplitude (phase). By repeating this measurement for different locations (Fig. 1b, empty spheres and
97 Extended Data Fig. 2), we can consistently classify the spectral response into one of these three
98 categories. The response across a grain boundary and on a thinner PbI_2 nano-island is discussed in
99 Extended Data Fig. 3.

100 The origin of the different signatures can be understood by relating our data with the local dielectric
101 response of the sample. We model the dielectric function of the unilluminated perovskite with a constant
102 background superimposed with Lorentzian oscillators (Fig. 1e, bottom row) that account for the strong
103 low-frequency phonons in the material; using the finite-dipole model we then arrive at the response
104 shown by dashed lines in the top two rows. For the left column in Fig. 1e, the spectral amplitude and
105 phase can be accurately reproduced by a dielectric function encompassing two Lorentzian oscillators

centred at 0.93 and 1.72 THz. This response is typical of the photoactive cubic perovskite α-phase (Fig. 1e, inset), where the low- and high-frequency Lorentzian oscillator can be attributed to a stretching and bending mode of the PbI_3 network, respectively (Methods and Extended Data Fig. 4). For the central column, the best agreement is obtained using two Lorentzian oscillators centred at 1.66 and 2.45 THz, which can be assigned to an I-Pb-I bending/stretching mode and a shearing mode of the PbI_3 octahedra of the non-perovskite δ-phase, respectively (Methods). Finally, the single Lorentzian observed in the right column at 1.75 THz is characteristic of a I-Pb-I bending mode in PbI_2 (Methods). To further corroborate our analysis, we directly extract the dielectric function from the experimental data by numerically inverting the finite-dipole model[39,40] (Fig. 1e, bottom row, full spheres). The excellent agreement with the analytical model confirms the assignment of the response to the cubic perovskite α-phase, trigonal δ-phase and PbI_2, respectively. Thus, our measurement of the local dielectric function of metal halide perovskites enables us to non-invasively identify their nanoscale crystallographic phase and chemical composition by phonon fingerprinting.

In-situ nanovideography of ultrafast electronic dynamics

Next, we extend nano-spectroscopy to ultrafast time scales to investigate how the local crystallographic configuration affects electron-hole (*e–h*) pair dynamics, such as recombination and diffusion. Therefore, we photogenerate *e-h* pairs using one-photon interband excitation with optical pump pulses (centre wavelength, 515 nm; pulse duration, 140 fs) and stroboscopically probe them by the evanescent THz near field (Fig. 2a, inset), polarising the *e-h* pairs. This provides a direct measure of the photo-induced charge-carrier density in the probing volume (Methods and Extended Data Fig. 5). Figure 2a shows the photo-induced change of the scattered THz waveform, ΔE_1, from an α-phase region (Fig. 1b, inset, blue sphere) at a delay time $t_\mathrm{p} = 11\,\mathrm{ps}$ after photoexcitation. The peak amplitude of ΔE_1 amounts to approximately 2×10^{-3} of the total scattered field E_1, attesting to the excellent experimental sensitivity. The pump-induced waveform shows enhanced trailing oscillations, indicating that the photoinjected *e-h* plasma screens the phonon resonances[42].

For a quantitative analysis, we consider the pump-induced spectral amplitude and phase referenced to the total scattered field $\Delta\tilde{E}_2/\tilde{E}_2$ (Fig. 2b, top panel) and $\Delta\phi_2 - \phi_2$ (bottom panel), respectively. Both

quantities display prominent features at 1 THz, explaining the pronounced oscillations in the time domain (Fig. 2a). Furthermore, a strictly positive background is measured in the spectral amplitude, characteristic of the broadband response of the photoexcited *e-h* plasma. By extending the dielectric function of the perovskite α-phase (Fig. 1e) by a Drude response (Methods), we can reproduce the features of the experiment with the multilayer finite-dipole model (Fig. 2b, dashed lines, Methods). No modification of the phonon contribution is required, indicating that phonon anharmonicities are not a dominant mechanism. On the PbI_2 protrusion (Fig. 1b, inset, green sphere) similar features are found (Fig. 2b, green spheres), with an overall reduced amplitude. Intriguingly, this response can be qualitatively reproduced by modelling a 60 nm thin layer of PbI_2 on top of the perovskite α-phase. Considering the lower absorption coefficient of PbI_2 compared to α-phase $FA_{0.83}Cs_{0.17}Pb(I_{1-x}Cl_x)_3$ (Methods), this observation suggests that the response is dominated by the material underneath the PbI_2 protrusion, showing the depth-sensitivity of our technique.

This picture is further corroborated by the temporal evolution of the peak of the photo-induced waveform $\Delta\hat{E}_1$ ($t_{\mathrm{eos}} = -50$ fs, Fig. 2c), which can be understood as a measure for the dynamics of the photogenerated *e-h* pair density within the near-field volume. For the perovskite α-phase, the signal rises within the femtosecond response time of our setup and decays to ~75% of its maximum value within our measurement window. Comparable dynamics are observed on the PbI_2 protrusion, yet the overall amplitude is only ~60% of the signal measured on the α-phase. In combination with the spectral signatures (Fig. 2b) and the weak absorption in PbI_2, we conclude that this signal predominantly originates from α-phase perovskite buried underneath the PbI_2 protrusion.

Changes of the *e-h* pair density can originate from recombination and diffusion. To distinguish these scenarios, we develop a novel depth-sensitive approach that maps minute pump-induced time shifts of the scattered THz waveform onto the spatial profile of the *e-h* pair density. Figure 3a shows the main cycle of the pump-induced waveform ΔE_1 for $t_{\mathrm{p}} = 9$ ps (violet spheres) and $t_{\mathrm{p}} = 509$ ps (red spheres). Intriguingly, the two waveforms have the same shape, but are slightly time-shifted. To quantify this shift, we fit a Gaussian wave packet to the transient taken at $t_{\mathrm{p}} = 9$ ps (violet line) and rigidly translate it along t_{eos} to fit the transient recorded at $t_{\mathrm{p}} = 509$ ps (red line). By extracting the zero-crossing t_0

(dashed vertical lines) with respect to $t_{\mathrm{eos}} = 0$ fs, we obtain a deeply subcycle time shift of (36 ± 4) fs; the error corresponds to only 0.6% of a THz cycle. A monotonic growth of t_0 with t_{p} is consistently observed on all parts of the sample. Figure 3b illustrates the situation at a different location. For early delay times, t_0 rapidly increases, whereas this trend slows down for later delay times.

Intriguingly, we can show that the observed subcycle shifts are microscopically linked to the out-of-plane carrier diffusion close to the surface of the sample, since the evanescent THz near field is particularly sensitive to charge carrier dynamics confined closely below the tip. As charge carriers diffuse into the bulk of the sample, the spatial profile of the dielectric function changes, leading to a phase shift between the scattered waveforms recorded at different pump delay times. For a quantitative understanding, we model the perovskite film as a stack of 100 layers (Fig. 3c) with their static dielectric function extracted in Fig. 1e for the perovskite α-phase; the photo-induced response is modelled by an additional Drude term with parameters extracted from Fig. 2b. Each layer is assigned an individual *e-h* pair density *n*. Right after photoexcitation, the density is assumed to decay monoexponentially into the sample according to the Lambert-Beer law (pump absorption length, 58 nm, see Methods). Subsequently, the density profile is modified by diffusion between neighbouring layers as well as mono- and bimolecular recombination accounting for trap-mediated and radiative recombination, respectively, as well as by Auger recombination, which is included for completeness. This leads to the following rate equation for the *e-h* pair density

$$\frac{\mathrm{d}n}{\mathrm{d}t} = D\,\frac{\mathrm{d}^2 n}{\mathrm{d}z^2} - k_1\,n - k_2\,n^2 - k_3\,n^3$$

where the bimolecular coefficient $k_2 = 12.6 \times 10^{-10}\mathrm{cm}^3\mathrm{s}^{-1}$ and the Auger coefficient $k_3 = 1 \times 10^{-30}\mathrm{cm}^6\mathrm{s}^{-1}$ are taken from far-field THz studies of identical samples[36] and the monomolecular coefficient k_1 is adapted to 10^9 s^{-1} for consistency with the observed charge-carrier recombination dynamics. The diffusion coefficient *D*, which is the only free model parameter, is varied between 0.1 and 1 $\mathrm{cm}^2\mathrm{s}^{-1}$ – a range consistent with optical far-field studies[22,23].

Using the finite-dipole model, we compute the evolution of t_0 for different diffusion coefficients (Fig. 3b, grey dashed lines), where the effect of photon reabsorption is found to be negligible in our

experimental configuration (Methods and Extended Data Fig. 6). The experimental data are excellently reproduced for $D = 0.3\ \mathrm{cm^2 s^{-1}}$, corresponding to a mobility of $\mu = 11.6\ \mathrm{cm^2 (Vs)^{-1}}$ (Fig. 3b, blue dashed line). The approach of modelling the carrier decay and diffusion for the previously extracted dielectric functions allows us to determine the vertical charge-carrier distribution with nanometre precision (Methods, Fig. 3d). The initial mono-exponential distribution (pink curve, $t_\mathrm{p} = 0$ ps) undergoes the strongest change for small pump delay times, explaining the strong initial change of t_0 (Fig. 3b). At later t_p, the distribution begins to equilibrate, reducing the rate of change observed in t_0. The robustness of our depth profiling is confirmed with a reference experiment on silicon (Methods and Extended Data Fig. 7) and a systematic evaluation of the role of the recombination coefficients and the initial density in our model (Methods and Extended Data Fig. 8).

To study the impact of topographic irregularities on the local vertical dynamics we repeat the experiments on perovskite crystallites of various sizes, grain boundaries, and a PbI_2 protrusion, in a different region of the same sample (Fig. 4a). The corresponding evolution of t_0 (Fig. 4b) is similar to the dynamics of Fig. 3b, for all locations. For the large crystallite (first panel) the dynamics can be reproduced with $D = 1\ \mathrm{cm^2 s^{-1}}$ ($\mu = 38.7\ \mathrm{cm^2 (Vs)^{-1}}$). Remarkably, the same value is also found for smaller grains and even on grain boundaries (second panel). On the PbI_2 island (third panel), t_0 exhibits a qualitatively similar shape residing on an overall offset. The latter can be accurately modelled by including an unexcited PbI_2 layer of a topographically determined thickness of 40 nm on top of a layer of the perovskite α-phase with the same diffusion coefficient of $D = 1\ \mathrm{cm^2 s^{-1}}$. This scenario is in line with the observation that the characteristic dispersive feature of the photoexcited perovskite α-phase is visible even on the PbI_2 protrusion (see discussion of Fig. 2). The latter increases the distance of the tip apex from the photoactive α-phase, introducing an additional offset in t_0.

These findings are corroborated by a line scan of t_0 in another sample area (Fig. 4c, Extended Data Fig. 9a). Similar to the results in Fig. 4b, different offsets are observed on grains with and without PbI_2 protrusions (Extended Data Fig. 9b for phonon fingerprinting), however, the diffusion is mostly encoded in the relative time shifts between early and late delay times. Hence, we can use straightforward mapping (Extended Data Fig. 9c) to extract the local diffusion constant as a function of position (Fig. 4d). We

obtain a uniform diffusion coefficient of $D = (0.2 \pm 0.1)\ \mathrm{cm^2 s^{-1}}$. Throughout the investigated regions, we measure locally uniform diffusion coefficients, regardless of topographic irregularities such as differently sized grains, grain boundaries or surface contaminations, implying that on length scales of multiple hundreds of nanometres, out-of-plane charge-carrier diffusivity is not strongly impeded by vertical grain boundaries visible at the sample surface. Conversely, the value of $D = 1\ \mathrm{cm^2 s^{-1}}$ observed in Fig. 4b significantly exceeds the one measured for the regions studied in Fig. 3b ($D = 0.3\ \mathrm{cm^2 s^{-1}}$) and Fig. 4d ($D \approx 0.2\ \mathrm{cm^2 s^{-1}}$). This might stem from the fabrication process[36], where upon nucleation pillars form that can be fully connected (enabling large diffusion coefficients, e.g., $D = 1\ \mathrm{cm^2 s^{-1}}$) or feature boundaries in the out-of-plane direction with limited $D \approx 0.3\ \mathrm{cm^2 s^{-1}}$. Our findings show that in $FA_{0.83}Cs_{0.17}Pb(I_{1-x}Cl_x)_3$ significant variations in the diffusion dynamics only occur on length scales larger than multiple hundreds of nanometres.

Discussion

In conclusion, we have simultaneously accessed the nanoscale crystallographic phase, chemical composition, and photo-induced electron dynamics in metal halide perovskite films. Deep-subcycle time shifts of the THz near field unveil the temporal evolution of the vertical density profile of photoexcited *e-h* pairs. On all measured locations, carrier diffusion is surprisingly immune to nanoscale variations in nano-morphology and chemical composition. A long list of further key open questions may now finally become solvable with ultrafast and structurally sensitive stroboscopic nano-videography. Examples include the charge-collection process at extraction layers, the microscopic origin of mesoscopic fluctuations of carrier diffusion, the role of defects at boundaries (Extended Data Fig. 10) or even in-plane charge transport. They are all vital for further improvements of fabrication protocols, but also for polaronic coupling of charge carriers with domain-specific phonons, and the effect of hot carriers or surface plasmons on the local dynamics. Solving these puzzles could unlock the full potential of perovskite materials for next-generation solar cells. Similarly, all nanophotonic and optoelectronic device development using nanocrystalline materials may immensely benefit from in-situ linking of nano-morphology and charge-carrier dynamics.

Acknowledgements

We thank M. Furthmeier for technical assistance. The work in Regensburg has been funded by the Deutsche Forschungsgemeinschaft (DFG, German Research Foundation) through projects 314695032 — SFB 1277 (sub-project A05), 277164313, and 326843318 as well as through research grant HU1598/8 (M.Z., S.N., F. Sandner, F. Schiegl, C.M., Y.A.G., T.S., M.A.H., R.H.). We thank the EPSRC (UK) for financial support through grants EP/T025077/1 and EP/V010840/1 (Q.Y., K.B.L., L.M.H., T.S., M.B.J.). M.B.J. is grateful to the Alexander von Humboldt Stiftung for a Friedrich Wilhelm Bessel Research Award which facilitated this project. Q.Y. acknowledges the support of Rank Prize through a Return to Research grant.

Author contributions

M.A.H., M.B.J. and R.H. conceived and supervised the study. M.Z., S.N., F. Sandner, F. Schiegl, C.M., Y.A.G., T.S., and M.A.H. performed the experiments and analysed the data. Q.Y., K.B.L., L.M.H. and M.B.J. fabricated the samples. All authors contributed to the discussions of the results. M.Z., S.N. and M.A.H. computed the multilayer scattering model. The manuscript was written by M.Z., S.N., T.S., M.A.H., M.B.J., and R.H. with input and contributions from all authors.

Corresponding authors

Correspondence to M.A.H. (markus.huber@ur.de), T.S. (thomas.siday@physics.ox.ac.uk), or M.B.J. (michael.johnston@physics.ox.ac.uk).

Competing interests

The authors declare no competing interests.

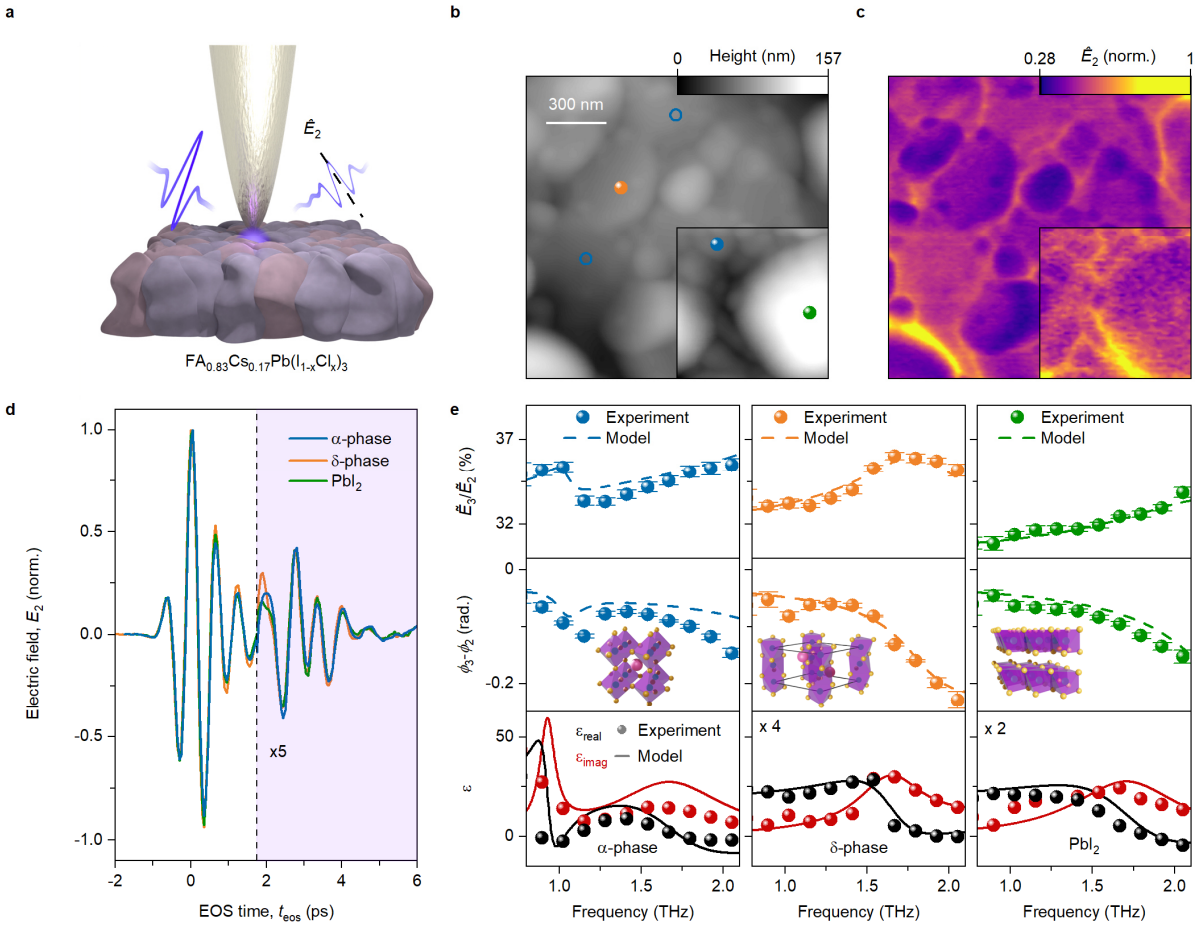

Figure 1 | Probing the chemical and crystallographic nano-morphology of metal halide perovskites with THz near-field spectroscopy. a, Schematic illustration of THz nano-spectroscopy. A THz pulse is coupled into evanescent near fields at the apex of a metallic tip placed above the surface of a $FA_{0.83}Cs_{0.17}Pb(I_{1-x}Cl_x)_3$ film on a *z*-cut quartz substrate. Analysing the scattered THz waveform yields access to the nanoscale dielectric response, allowing us to infer the nanoscale chemical composition and crystal structure. **b,** Atomic force microscopy image of the perovskite surface, exhibiting typical nanoscale grains. The coloured spheres indicate the positions of spectroscopic measurements conducted in **d**, **e** and Extended Data Fig. 2. Inset: topography map of a different part of the sample. **c,** Corresponding amplitude at the peak of the steady-state scattered THz electric field $\hat{E}_2$ (see dashed line in **a**). The signal at grain boundaries is generally increased whereas grains show an overall lower scattering response, varying slightly in amplitude. Inset: $\hat{E}_2$ map of a different part of the sample. **d,** Scattered THz waveform E_2 recorded on the positions marked by the full spheres in **b**. At late electro-optic sampling (EOS) times t_{eos} the vertical axis is stretched to highlight the differences in the trailing

oscillations of the scattered transients between the different locations. **e,** Spectroscopic investigation of the chemical composition and crystallographic phase of the perovskite film. The spectral amplitude (top row) and phase (middle row) of the third demodulation order relative to the second ($\tilde{E}_3/\tilde{E}_2$ and $\phi_3 - \phi_2$) reveal three qualitatively different responses on the sample, which can be attributed to the perovskite α-phase (blue), the non-perovskite δ-phase (orange) and PbI_2 (green). Overlayed are fits obtained with the finite-dipole model. The underlying dielectric functions retrieved from the model are shown in the bottom row, along with the respective dielectric functions extracted directly by inverting the finite-dipole model. The data in the top two rows in **e** are shown as mean values of 12, 5, and 8 measurements for the α-phase, the δ-phase, and PbI_2, respectively, and the error bars indicate the corresponding standard errors.

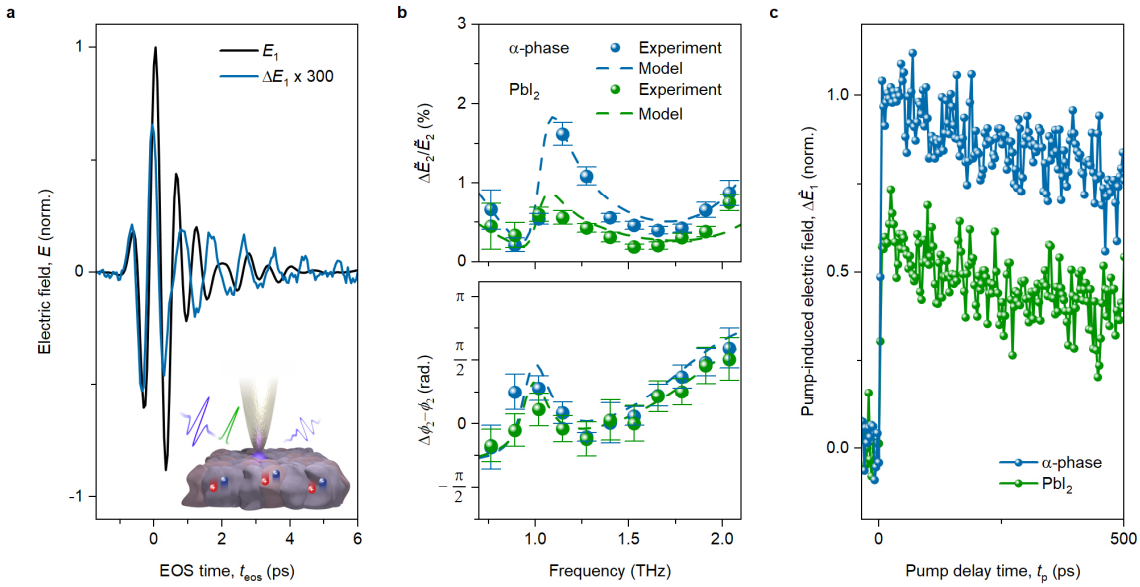

Figure 2 | Pump-induced near-field response of the perovskite film. a, Steady-state (E_1, black) and photo-induced (ΔE_1, $t_p = 11$ ps, blue) THz near-field waveform at the first demodulation order on a position identified as the α-phase. The pronounced trailing oscillations in ΔE_1 indicate a significant interaction through screening between the photoexcited electron-hole plasma and phonons. Inset: Ultrafast depth-sensitive near-field nanoscopy. An optical pump pulse (photon energy, 2.4 eV; pulse duration, 140 fs; fluence, 14.5 μJ cm^{-2}) photo-generates electron-hole pairs, which are subsequently polarised by the evanescent THz near field. Thereby, charge-carrier dynamics such as diffusion and recombination can be inferred. **b,** Relative photo-induced change to the spectral amplitude ($\Delta\tilde{E}_2/\tilde{E}_2$, top panel) and phase ($\Delta\phi_2 - \phi_2$, bottom panel) at the second demodulation order recorded on the α-phase (blue) and on a PbI_2 protrusion (green) 11 ps after photoexcitation, both marked in the inset of Fig. 1b. Phonons in the α-phase lead to strong dispersive features even on the PbI_2 protrusion, where the α-phase perovskite below the contamination dominates the response. The shape of the experimental data can be accurately reproduced by a multilayer finite-dipole model (dashed lines, see Methods). The modelled spectral amplitude is rescaled by a factor of 0.8. The data are shown as mean values of 19 measurements per spectrum and the error bars represent the corresponding standard error. **c,** Peak of the pump-induced signal at the first demodulation order $\Delta\hat{E}_1$ ($t_{eos} = -50$ fs) as a function of pump delay time t_p for both positions. The curve taken on the PbI_2 protrusion shows a similar decay behaviour as the one taken on

304 the α-phase with an overall lower amplitude. Along with the results of **b**, this indicates that the signal is
305 dominated by buried α-phase perovskite.

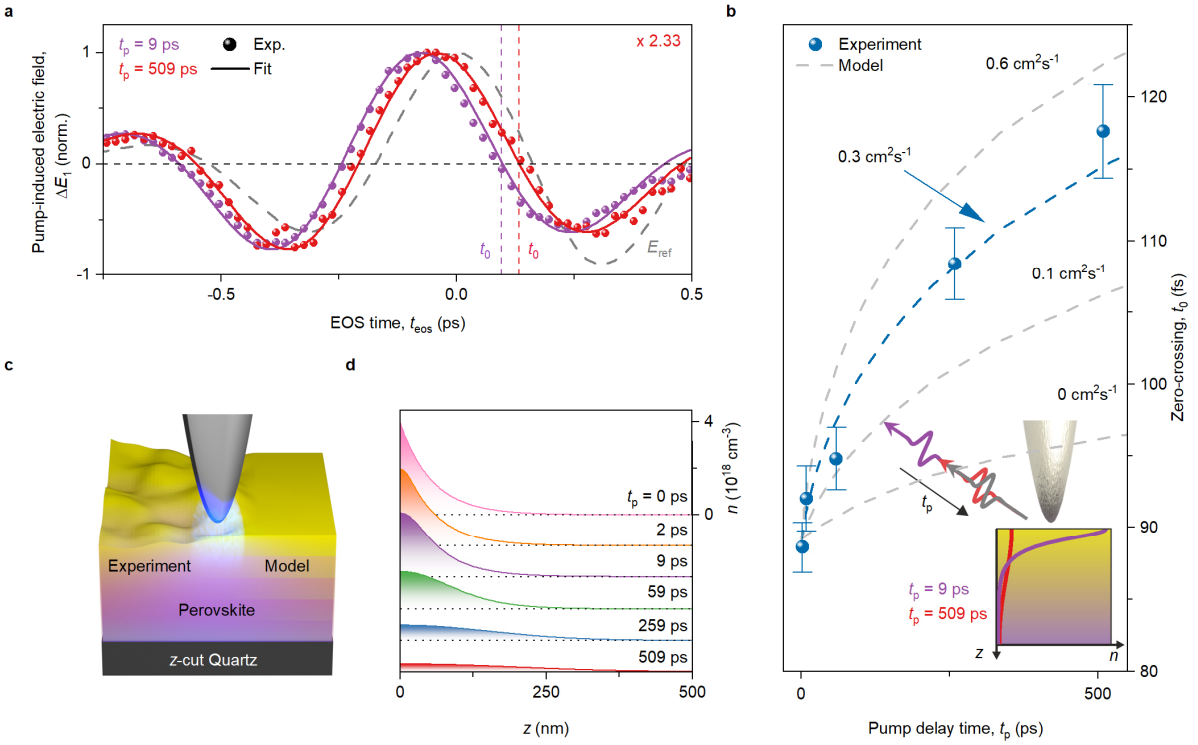

306

307 **Figure 3 | Quantifying the out-of-plane charge-carrier diffusion in a perovskite film. a,** Main
308 oscillation cycle of the pump-induced THz waveform ΔE_1 for $t_p = 9$ ps (violet spheres) and $t_p =$
309 509 ps (red spheres). The two transients exhibit a nearly identical shape and only differ in their shift
310 with respect to EOS time $t_{eos} = 0$ ps. To quantify this time shift, the data has been fit with the product of
311 a Gaussian and a sine function (full lines) and the zero-crossing of the respective fits have been extracted
312 (vertical dashed lines). The dashed grey waveform indicates the unexcited near-field response for the
313 second demodulation order to highlight the direction of the time shift. **b,** Change in the first zero-
314 crossing after the peak of the ΔE_1 waveform as a function of pump delay time t_p. We can model these
315 shifts using the approach discussed in the Methods section for different out-of-plane diffusion
316 coefficients (dashed lines), where the best agreement is found for $D = 0.3$ cm^{2}s^{-1}. Each data point and
317 error bar indicates the zero-crossing and the 68% confidence interval, respectively, extracted by a
318 parametric fit (Methods) to a pump-induced THz waveform ΔE_1 consisting of 22 data points, each
319 averaged across 3 measurements. Inset: Intuitive picture of origin of time shift. After photoexcitation,
320 the steep depth-profile of the charge-carrier density (purple, $t_p = 9$ ps) leads to a strong shift of the
321 transient compared to the reference transient (black). Diffusion leads to an almost depth-independent

distribution, causing the evolution of t_0 to saturate. **c,** Visualisation of the model. The sample is discretised into 100 layers, each featuring a different dielectric function according to a straightforward diffusion model. The scattering response is then obtained from a multilayer finite-dipole model (see results in **b**). **d,** Vertical profile of the three-dimensional charge-carrier density in the material determined by the diffusion model for a diffusion coefficient of D = 0.3 cm^2s^{-1} for different delay times after photoexcitation.

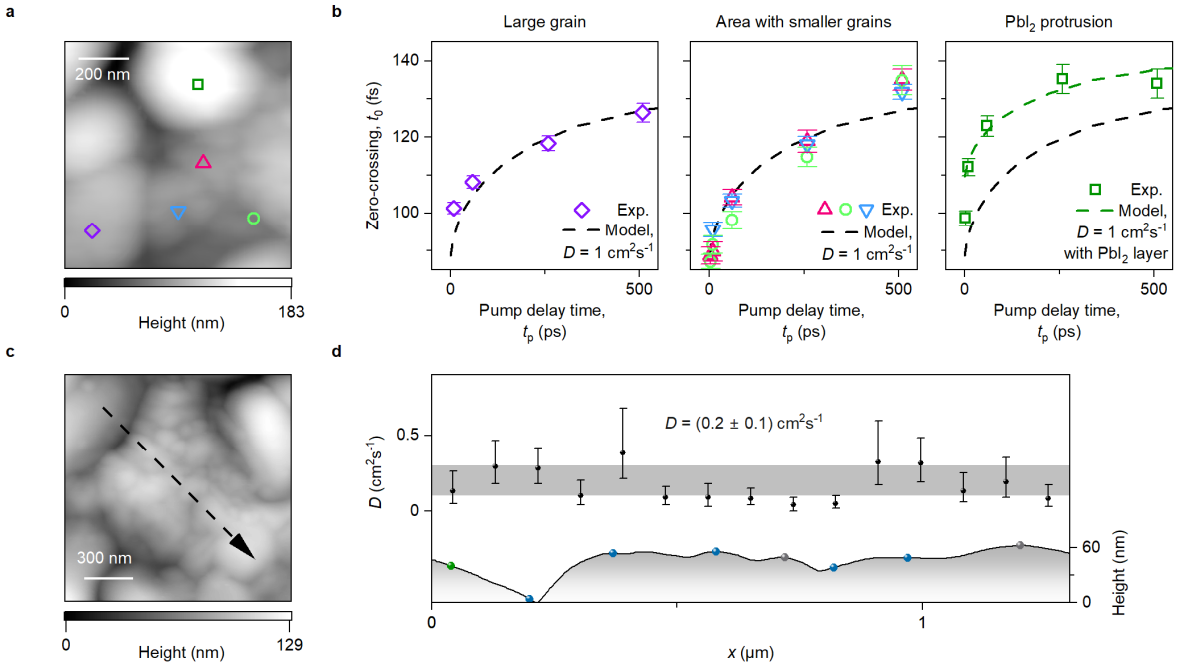

328

329 **Figure 4 | Position dependence of the out-of-plane charge-carrier diffusion in different regions of**
330 **the perovskite sample. a,** Topography map of the investigated region on the same sample as in Fig. 3,
331 where the positions for the measurements of the local charge-carrier dynamics are indicated by the
332 coloured symbols. **b,** Extracted shift of the zero-crossing t_0 of ΔE_1 as a function of pump delay time t_p.
333 A qualitatively similar behaviour can be observed on all positions. The values of t_0 acquired on a large
334 crystallite (first panel, violet), smaller crystallites (second panel, blue and pink) and even a grain
335 boundary (second panel, lime) can be modelled with a diffusion coefficient of $D = 1\ \mathrm{cm^2 s^{-1}}$ (black
336 dashed lines). At the location on the PbI_2 protrusion, we observe an offset in t_0 (third panel, green),
337 which we can model with a layer of the perovskite α-phase ($D = 1\ \mathrm{cm^2 s^{-1}}$) covered by a 40-nm-thin
338 layer of PbI_2 (green dashed line). Each data point and error bar indicates the zero-crossing and the 68%
339 confidence interval, respectively, extracted by a parametric fit (Methods) to a pump-induced THz
340 waveform ΔE_1 consisting of 74 (29) data points, each averaged across 3 measurements for the positions
341 marked by the purple and cyan (dark green, bright green and red) symbol. **c,** Topography map of a
342 different region. **d,** Extracted diffusion coefficient along the black dashed line in **c** (Extended Data Fig.
343 9a,c). The coloured spheres superimposed on the height profile indicate the locations where spectra of
344 the unexcited sample were recorded to identify the chemical composition/crystallographic phase of the
345 respective grain. Blue spheres indicate α-phase perovskite, green means PbI_2 and grey represents a
346 mixed phase (Extended Data Fig. 9b). The data show the diffusion coefficient whereas the error bars

represent the 68% confidence interval retrieved by directly mapping the uncertainty in the position of the zero-crossing onto the diffusion coefficient according to Extended Data Fig. 9c. Further statistics: see Extended Data Fig. 9a.

References

1. Kojima, A., Teshima, K., Shirai, Y. & Miyasaka, T. Organometal halide perovskites as visible-light sensitizers for photovoltaic cells. *J. Am. Chem. Soc.* **131**, 6050–6051 (2009).

2. Lee, M. M., Teuscher, J., Miyasaka, T., Murakami, T. N. & Snaith, H. J. Efficient Hybrid Solar Cells Based on Meso-Superstructured Organometal Halide Perovskites. *Science* **338**, 643–647 (2012).

3. Kim, H.-S. et al. Lead Iodide Perovskite Sensitized All-Solid-State Submicron Thin Film Mesoscopic Solar Cell with Efficiency Exceeding 9%. *Sci. Rep.* **2**, 591 (2012).

4. Stranks, S. D. et al. Electron-Hole Diffusion Lengths Exceeding 1 Micrometer in an Organometal Trihalide Perovskite Absorber. *Science* **342**, 341–344 (2013).

5. Liu, M., Johnston, M. B. & Snaith, H. J. Efficient planar heterojunction perovskite solar cells by vapour deposition. *Nature* **501**, 395–398 (2013).

6. Wehrenfennig, C., Eperon, G. E., Johnston, M. B., Snaith, H. J. & Herz, L. M. High charge carrier mobilities and lifetimes in organolead trihalide perovskites. *Adv. Mater.* **26**, 1584–1589 (2014).

7. Shi, D. et al. Low trap-state density and long carrier diffusion in organolead trihalide perovskite single crystals. *Science* **347**, 519–522 (2015).

8. Eperon, G. E. et al. Perovskite-perovskite tandem photovoltaics with optimized band gaps. *Science* **354**, 861–865 (2016).

9. Yoo, J. J. et al. Efficient perovskite solar cells via improved carrier management. *Nature* **590**, 587–593 (2021).

10. Min, H. et al. Perovskite solar cells with atomically coherent interlayers on SnO_2 electrodes. *Nature* **598**, 444–450 (2021).

11. Sun, Y. et al. Bright and stable perovskite light-emitting diodes in the near-infrared range. *Nature* **615**, 830-835 (2023).

12. Lin, K. et al. Perovskite light-emitting diodes with external quantum efficiency exceeding 20 per cent. *Nature* **562**, 245–248 (2018).

13. Feng, J. et al. Single-crystalline layered metal-halide perovskite nanowires for ultrasensitive photodetectors. *Nat. Electron.* **1**, 404–410 (2018).

14. Zhu, H. et al. Lead halide perovskite nanowire lasers with low lasing thresholds and high quality factors. *Nat. Mater.* **14**, 636–642 (2015).

15. Huang, C. et al. Ultrafast control of vortex microlasers. *Science* **367**, 1018–1021 (2020).

16. NREL. Best Research-Cell Efficiencies. https://www.nrel.gov/pv/cell-efficiency.html (accessed 2024-05-15).

17. Xue, J., Wang, R. & Yang, Y. The surface of halide perovskites from nano to bulk. *Nat. Rev. Mater.* **5**, 809–827 (2020).

18. Stoumpos, C. C., Malliakas, C. D. & Kanatzidis, M. G. Semiconducting tin and lead iodide perovskites with organic cations: Phase transitions, high mobilities, and near-infrared photoluminescent properties. *Inorg. Chem.* **52**, 9019–9038 (2013).

19. Szostak, R. et al. Nanoscale mapping of chemical composition in organic-inorganic hybrid perovskite films. *Sci. Adv.* **5**, eaaw6619 (2019).

20. Rothmann, M. U. et al. Atomic-scale microstructure of metal halide perovskite. *Science* **370**, eabb5940 (2020).

21. Guo, Z., Manser, J. S., Wan, Y., Kamat, P. V. & Huang, L. Spatial and temporal imaging of long-range charge transport in perovskite thin films by ultrafast microscopy. *Nat. Commun.* **6**, 7471 (2015).

22. Cho, C. et al. Efficient vertical charge transport in polycrystalline halide perovskites revealed by four-dimensional tracking of charge carriers. *Nat. Mater.* **21**, 1388–1395 (2022).

23. Feng, M., Ye, S., Guo, Y. & Sum, T. C. Intrinsic Carrier Diffusion in Perovskite Thin Films Uncovered by Transient Reflectance Spectroscopy. *Nano Lett.* **22**, 7195–7202 (2022).

400 24. Righetto, M. et al. Hot carriers perspective on the nature of traps in perovskites. *Nat. Commun.*
401 **11**, 2712 (2020).

402 25. Eisele, M. et al. Ultrafast multi-terahertz nano-spectroscopy with sub-cycle temporal
403 resolution. *Nat. Photonics* **8**, 841–845 (2014).

404 26. Wagner, M. et al. Ultrafast and Nanoscale Plasmonic Phenomena in Exfoliated Graphene
405 Revealed by Infrared Pump–Probe Nanoscopy. *Nano Lett.* **14**, 894–900 (2014).

406 27. Ni, G. X. et al. Ultrafast optical switching of infrared plasmon polaritons in high-mobility
407 graphene. *Nat. Photonics* **10**, 244–247 (2016).

408 28. Huber, M. A. et al. Femtosecond photo-switching of interface polaritons in black phosphorus
409 heterostructures. *Nat. Nanotechnol.* **12**, 207–211 (2017).

410 29. Sternbach, A. J. et al. Programmable hyperbolic polaritons in van der Waals semiconductors.
411 *Science* **371**, 617–620 (2021).

412 30. Nishida, J. et al. Nanoscale heterogeneity of ultrafast many-body carrier dynamics in triple
413 cation perovskites. *Nat. Commun.* **13**, 6582 (2022).

414 31. Plankl, M. et al. Subcycle contact-free nanoscopy of ultrafast interlayer transport in atomically
415 thin heterostructures. *Nat. Photonics* **15**, 594–600 (2021).

416 32. Pizzuto, A. et al. Nonlocal Time-Resolved Terahertz Spectroscopy in the Near Field. *ACS*
417 *Photonics* **8**, 2904–2911 (2021).

418 33. Zhang, J. et al. Terahertz Nanoimaging of Graphene. *ACS Photonics* **5**, 2645–2651 (2018).

419 34. Kim, R. H. J. et al. Terahertz Nanoimaging of Perovskite Solar Cell Materials. *ACS Photonics*
420 **9**, 3550–3556 (2022).

421 35. Klarskov, P., Kim, H., Colvin, V. L. & Mittleman, D. M. Nanoscale Laser Terahertz Emission
422 Microscopy. *ACS Photonics* **4**, 2676–2680 (2017).

423 36. Lohmann, K. B. et al. Solvent-Free Method for Defect Reduction and Improved Performance

of p-i-n Vapor-Deposited Perovskite Solar Cells. *ACS Energy Lett.* **7**, 1903–1911 (2022).

37. Maeng, I. et al. Unusual terahertz-wave absorptions in δ/α-mixed-phase $FAPbI_3$ single crystals: interfacial phonon vibration modes. *NPG Asia Mater.* **13**, 75 (2021).

38. Siday, T. et al. Ultrafast Nanoscopy of High-Density Exciton Phases in WSe_2. *Nano Lett.* **22**, 2561–2568 (2022).

39. Govyadinov, A. A. et al. Recovery of Permittivity and Depth from Near-Field Data as a Step toward Infrared Nanotomography. *ACS Nano* **8**, 6911–6921 (2014).

40. Mooshammer, F. et al. Nanoscale Near-Field Tomography of Surface States on $(Bi_{0.5}Sb_{0.5})_2Te_3$. *Nano Lett.* **18**, 7515–7523 (2018).

41. Babicheva, V. E., Gamage, S., Stockman, M. I. & Abate, Y. Near-field edge fringes at sharp material boundaries. *Opt. Express* **25**, 23935 (2017).

42. Wright, A. D. et al. Electron-phonon coupling in hybrid lead halide perovskites. *Nat. Commun.* **7**, 11755 (2016).

Methods

Sample fabrication. The $FA_{0.83}Cs_{0.17}Pb(I_{1-x}Cl_x)_3$ thin-film samples were prepared as previously reported[36]: Cleaned quartz (UQG optics – saw grade, double sided polished, *z*-cut +/-15') substrates were O_2-plasma treated (10 minutes) prior to vapour co-deposition in our custom-built thermal evaporator. Thin films (thickness, ~500 nm) were co-deposited from precursors of $CH(NH_2)_2I$, PbI_2, $PbCl_2$, and CsI under high vacuum with a pressure of $<1 \times 10^{-6}$ mbar. The evaporation rates of each precursor were controlled such that there was a 20% substitution of PbI_2 for $PbCl_2$ (ref. 36). The $PbCl_2$ acts as a defect passivating agent, ruling out significant effects of halide segregation. After deposition, all samples were annealed on a hotplate at 135 °C for 30 minutes in N_2 atmosphere to form perovskites with the desired composition.

Setup for ultrafast depth-sensitive THz near-field nanoscopy. Our approach is based on THz near-field microscopy[31,38,43] with a high-power, low-noise Yb:YAG thin-disk laser oscillator[44], providing near-infrared pulses (pulse duration, 200 fs; centre wavelength, 1030 nm; pulse energy, 3.75 μJ; repetition rate, 24 MHz). Phase-stable THz pulses (average power, 1.2 mW; spectral components two orders of magnitude above the noise floor range from 0.9 to 2 THz) are generated by optical rectification in a 2-mm-thick GaP (110) crystal. A second laser branch is acousto-optically modulated at a frequency of 110 kHz and frequency-doubled in a β-barium borate crystal (thickness, 1.2 mm; angle of cut, 23.4°) to provide pump pulses at a centre wavelength of 515 nm. Alternatively, the laser fundamental can be used for photoexcitation. The pump and probe pulses are focused onto the tip (25PtIr200BH, Rocky Mountain Nanotechnology, LLC) of a commercial near-field microscope. The electric field of the scattered probe pulses is detected using electro-optic sampling in a GaP crystal, gated by the laser fundamental. To eliminate far-field background, a lock-in amplifier demodulates the detected signal either at the j^{th} harmonic of the tip tapping frequency or, for pump-probe measurements, at the first positive sideband to the j^{th} harmonic originating from the pump modulation[31,38].

Equilibrium scans were acquired within ~40 to ~100 min (Figs. 1b-e). Full waveforms under photoexcitation (Fig. 2a and b) and the pump probe trace (Fig. 2c) took ~150 min and ~9 min, respectively. For the extraction of the time shifts in Fig. 3 and 4, data acquisition times ranged from ~9

min to ~23 min per data point t_0. To reduce drift between tip and sample and avoid absorption of THz radiation by water vapor, we enclosed our near-field microscope in a nitrogen-purged, temperature-monitored, vibrationally isolated metal container. Taking AFM images before and after each scan, the drift can be quantified (~0.5 nm/minute or less), where it is always ensured that it plays no role for the interpretation of the results.

Details of the multilayer scattering model. To describe the near-field interaction of THz radiation with the tip-sample system, we employ the finite-dipole model[45,46], yielding the frequency-dependent complex scattering amplitude $\tilde{s}_j = \tilde{E}_j \times \mathrm{e}^{\mathrm{i}\varphi_j}$ for each demodulation order j. The pump-induced scattered signal is extracted from the model as $\Delta\tilde{s}_j = \Delta\tilde{s}_{j,\mathrm{photoexcited}} - \Delta\tilde{s}_{j,\mathrm{equilibrium}}$ with $\Delta\tilde{s}_{j,\mathrm{photoexcited}}$ ($\Delta\tilde{s}_{j,\mathrm{equilibrium}}$) being the modelled response of the photoexcited (equilibrium) sample. The multilayer scattering model is based on the procedure described in reference 46, where the potential response ϕ of a flat layered sample to the potential of a monopole Q at a distance z_0 is given by

$$\phi(z) = -\frac{Q}{4\pi\varepsilon_0}\int_0^\infty A(k)\,\mathrm{e}^{kz} J_0(kr)\mathrm{d}k = -\frac{Q}{4\pi\varepsilon_0}\int_0^\infty A'(k)\,\mathrm{e}^{kz}\mathrm{e}^{-2kz_0}\,J_0(kr)\mathrm{d}k$$

where ε_0 is the vacuum permittivity, J_0 is the first kind Bessel function of zeroth order, $A(k) = A'(k)\mathrm{e}^{-2kz_0}$, and $A'(k) = \frac{\beta_{12}+\beta_{23}e^{-2kd}}{1-\beta_{21}\beta_{23}e^{-2kd}}$ for a sample covered by one layer of thickness d. The quasistatic reflection coefficient β_{ij} is given by $\beta_{ij} = \frac{\varepsilon_i-\varepsilon_j}{\varepsilon_i+\varepsilon_j}$, where ε_i (ε_j) denotes the dielectric function of the i^{th} (j^{th}) layer. Appendix 6.1 of reference 46 shows that the coefficient $A'(k)$ corresponds to the negative quasistatic reflection coefficient $r_p(k)|_{q=0}$ with in-plane momentum q. Using $A'(k) = -r_p(k)|_{q=0}$ an extension to systems with an arbitrary number of layers is straightforward by calculating the Fresnel coefficient using a transfer matrix method[47]. The required input parameters are the tapping amplitude (80 nm), the tip radius of curvature (40 nm), the tip spheroid length 2L (720 nm), and the empirical geometry factor g ($0.7 \times \mathrm{e}^{0.06\mathrm{i}}$) in agreement with other studies[48,49]. Our sample is modelled as a layered system, with the top and bottom layer being infinite half-spaces of air and z-cut quartz with a dielectric function taken from literature[50], respectively. The metal halide perovskite samples are

modelled by a single layer with a thickness of 500 nm (Fig. 1) as determined from the fabrication protocols and a dielectric function as mentioned in the main text or as a layered stack (100 layers) to model depth-dependent density profiles (Fig. 2, 3 and 4). Each layer is ascribed an individual charge-carrier density. In Fig. 2b the charge-carrier distribution is set to an exponential distribution according to the Lambert-Beer law (penetration depth, ~58 nm). In Fig. 3 and 4, this initial charge-carrier distribution is altered according to the equation in the main text simulating the density-dependent recombination and diffusion. The equation is solved using a forward Euler method and no-flux boundary conditions are applied. When modelling the response on a PbI_2 protrusion, we add a layer to the sample stack with the dielectric function of PbI_2 as retrieved in Fig. 1e and a thickness extracted from an AFM topography map. Since the absorption length of our pump pulses in PbI_2 is larger than for the perovskite α-phase by approximately an order of magnitude[51], we neglect possible photoexcitation of the PbI_2.

Unnormalized waveforms and retraction scans. Extended Data Fig. 1 shows waveforms, spectra and retraction curves up to demodulation order $j = 3$ for locations identified as the perovskite α-phase and a PbI_2 protrusion, as well as a gold reference and a high-resistivity silicon wafer. Replica of the initial THz pulse can be identified at a delay of $t_{eos} \approx 2.6$ ps, originating from a reflection travelling along the cantilever[52]. In the frequency domain, they manifest as a periodic modulation of the spectral amplitude. Furthermore, normalised retraction curves are shown with a horizontal dashed line indicating a value of 1/e. Whereas the first demodulation order is not well confined spatially, all retraction curves of second and third demodulation order decay on length scales smaller than 50 nm and 20 nm, respectively. Therefore, equilibrium measurements preferentially use at least the second demodulation order.

For the first demodulation order under photoexcitation a 1/e decay length of ~130 nm can be extracted (excitation parameters identical to the final section of the Methods). The significantly faster decay of $\Delta\hat{E}_1$ compared to $\hat{E}_1$ can be attributed to the small spot size of the pump beam compared to the THz beam owing to a reduction of weakly distance-dependent background fields from areas away from the tip apex. Owing to side-band detection, contributions to the scattered signal originating from regions distant to the tip apex (which contribute to E_1) are removed in $\Delta\hat{E}_1$. Also in the second demodulation order the 1/e decay length decreases from ~45 nm for $\hat{E}_2$ to ~33 nm for $\Delta\hat{E}_2$.

Details on the fitting procedure of the equilibrium response. For the analysis of the spectra, for example, in Fig. 1e, different demodulation orders are divided to suppress contributions from indirect tip illumination[53] or Fabry-Pérot-like interferences from reflections off the cantilever[52] (see Extended Data Fig. 1). The spectra are modelled with the fitting routine described in ref. 53, where a real-valued offset between model and experiment is allowed. With this approach, we access the local dielectric function of the three observed chemical compositions/crystallographic phases. The dielectric functions are parametrised as the sum of a static dielectric background $\varepsilon_{\mathrm{static}}$ with one or two Lorentzian oscillators:

$$\varepsilon(\omega) = \varepsilon_{\mathrm{static}} + \sum_{\mathrm{k}} \frac{f_{\mathrm{k}}\omega_{\mathrm{res,k}}^2}{\omega_{\mathrm{res,k}}^2 - \omega^2 - \mathrm{i}\beta_{\mathrm{k}}\omega}$$

with resonant angular frequency $\omega_{\mathrm{res}} = 2\pi\upsilon_{\mathrm{res}}$, damping coefficient β_{k}, and oscillator strength f_{k}, for each oscillator k. All parameters with literature references are presented in Extended Data Fig. 4. Additionally, we invert the finite-dipole model similar to ref. 40 to directly extract the dielectric function from the experimental data without making assumptions on the nature of the spectrum.

Modelling the photo-induced response. To simulate the response of the photoexcited perovskite in the α-phase, a Drude term is added to its steady-state dielectric function describing the effect of photo-induced charge-carriers counteracting the polarization in the lattice by screening the equilibrium optical phonons[54]. This allows us to model the pump-induced change to the scattered signal using the multilayer finite-dipole model. The term is defined by

$$-\frac{{\omega_p}^2}{\omega^2 + \left(\omega \times \frac{2\pi\mathrm{i}}{\tau}\right)}$$

with a plasma frequency $\omega_p = \sqrt{\frac{ne^2}{\mu\varepsilon_0}}$, a Drude scattering time τ, a charge-carrier density n, the elementary charge e, a reduced effective mass μ, and the vacuum permittivity ε_0. We take the reduced effective mass of electron-hole pairs $\mu = ((0.218\, m_e)^{-1} + (0.273\, m_h)^{-1})^{-1} = 0.121\, m_e$ from literature[55]. Using literature values of THz far-field studies[36], we can estimate τ and thus the complete Drude susceptibility. The initial charge-carrier density of each layer (Fig. 3d,pink curve) used in the multilayer model is determined by estimating the photon fluence and assuming a conversion efficiency

of 100%. Specifically, we take the repetition rate of the laser, the focal spot size (FWHM 3.4 $\mu m \times$ 7.4 μm), the beam shape (Gaussian), the average optical power (100 µW), and the duty cycle of our acousto-optic modulator (50%) into account. This yields an upper limit of the pump fluence $\phi_{\max} =$ 29 µJ cm^{-2} at the tip apex. Since the focal spot below the tip cannot be determined with perfect accuracy, we estimate that the actual value in the experiment is $\phi = 14.5$ µJ cm^{-2} yielding optimal agreement with our simulations. To estimate the photon flux entering the sample, we account for reflections off the sample surface. We use a refractive index of $n_r = 2.5$ and an extinction coefficient of $k = 0.7$ in accordance with literature reports on $FA_{0.85}Cs_{0.15}PbI_3$ for a photoexcitation wavelength of $\lambda = 515$ nm (see ref. 56). Illumination appears under an incidence angle of 60° with respect to the tip. Thus, a reflectance $R_\mathrm{s} = |r_\mathrm{s}|^2 = 0.42$ for s-polarized light can be calculated considering the respective Fresnel coefficient r_s. Owing to strong absorption in $FA_{0.83}Cs_{0.17}Pb(I_{1-x}Cl_x)_3$ we assume full extinction of the non-reflected photons $A = 1 - R_\mathrm{s} = 0.58$. Using a penetration depth of ~58 nm and the Lambert-Beer law yields a distribution of $n(z)$:

$$n(z) = A \times \frac{\phi}{\epsilon_\mathrm{photon}} \times \frac{e^{-\alpha z \cos(\theta_\mathrm{r})^{-1}}}{\int_0^{500\,\mathrm{nm}} e^{-\alpha z \cos(\theta_\mathrm{r})^{-1}} \mathrm{dz}}.$$

Here, $\alpha = 4\pi k \lambda^{-1}$ is the absorption coefficient and $\epsilon_\mathrm{photon} = 2.4$ eV the photon energy of the pump. The expression $\cos(\theta_\mathrm{r})^{-1}$ accounts for the propagation direction of energy given by the Poynting vector which is not normal to the sample surface and depends on the angle of refraction $\theta_\mathrm{r} \approx 20°$ (calculated by Snell's law). To suppress the influence of in-plane diffusion in the experiment, the beam size of the pump spot is chosen such that a homogeneous initial carrier density distribution is generated on the relevant length scales. Additionally, since the data show no relevant dependence of the zero-crossings on the grain size or distance from grain boundaries (see Fig.4b, Extended Data Fig. 9a), we conclude that in-plane diffusion or trapping plays no crucial role for our results. To further study in-plane diffusion, our approach could be modified by choosing photoexcitation energies closer to the band gap, yielding larger absorption depths and thereby a flatter initial carrier density profile. This would isolate in-plane effects by suppressing out-of-plane diffusion.

Since the temporal shape of the photoexcited transients remains identical for all delay times (Extended Data Fig. 5a,b) and their amplitudes scale linearly with increasing fluence (Extended Data Fig. 5c), the peak of the pump-induced waveform $\Delta\hat{E}_1$ is a measure of the carrier density in the probing volume[57]. The local increase in average temperature of the sample during illumination with the pump beam is estimated to be less than 5 °C, rendering thermal effects insignificant.

Extracting and modelling the subcycle femtosecond time shifts. To extract the experimentally observed time shifts, we fit the main cycle of the pump-induced scattered waveform ΔE_1 by:

$$\Delta E_{1,\mathrm{fit}}(t) = \mathrm{A}\cos[\omega_{\mathrm{carrier}}(t - t_{\mathrm{offset}}) + \varphi]\, e^{-\frac{(t-t_{\mathrm{offset}})^2}{2\sigma^2}}$$

with amplitude A, carrier frequency $\omega_{\mathrm{carrier}}$, phase offset φ, temporal width σ, and temporal offset t_{offset}. For each dataset, the equation above is fit to the main oscillation cycle for the earliest measured pump delay time using a nonlinear least-squares approach. For all remaining pump delay times, only A and t_{offset} are adjusted to fit ΔE_1. This allows us to extract t_0 for all pump delay times t_p.

To obtain t_0 in the theoretical model, we start with the steady-state dielectric function extracted in Fig. 1e. When applying the finite-dipole model, we account for the effects of the input spectrum as follows: The complex output spectrum from the model is multiplied with a Gaussian, slightly adjusted for the different spectral response functions of the tips used in the experiment. For Figs. 3b and 4b (4d), we use a FWHM of 0.97 THz (0.99 THz), a centre frequency of 1.44 THz (1.41 THz), and a carrier-envelope-phase offset of $-0.51\,\pi$ ($-0.37\,\pi$). Subsequently, it is Fourier-transformed to fit the main oscillation cycle of the experimental THz transient E_1 where the detector response is also accounted for[31]. For the initial charge-carrier density, penetration depth, and Drude scattering time, we use identical parameters as assumed for the modelling of Fig. 2. The recombination parameters k_1, k_2 and k_3 are adapted from literature[36]. Auger recombination (k_3) is included, but does not play a significant role for our experimental conditions. The diffusion coefficient D remains the only free fitting parameter to individually model the measured subcycle time shifts in Fig. 3 and 4. The observed shift in the pump-induced waveforms is primarily determined by the vertical charge-carrier distribution, not the total number of charge carriers, corroborated by modelling the evolution of the zero-crossing for different

recombination parameters k_1, k_2, k_3 or fluence ϕ (Extended Data Fig. 8). Notably, the monomolecular, bimolecular, and Auger recombination coefficients or fluence need to be changed significantly (factors of 0 to 20 for k_1, 0 to 5 for k_2, 0 to 3000 for k_3 and 0.2 to 5 for ϕ) compared to the diffusion coefficient to obtain relevant effects on the shape of the evolution in the zero-crossings.

Thereby, the vertical density profile of *e-h* pairs can be inferred. We associate an effective depth of the charge carriers for each delay time t_p by taking the weighted arithmetic mean. The first and third data point in Fig. 3b can be clearly distinguished within the experimental error. Between these points a vertical change of ~22 nm can be extracted, yielding an estimate of the minimum resolution in the *z*-direction of the measurement. The values for the charge-carrier mobility given in the manuscript are calculated by $\mu = eD/(k_B T)$, with elementary charge e, Boltzmann constant k_B and a temperature of $T = 300$ K.

Effect of photon reabsorption. The effect of photon reabsorption[58] is negligible for the interpretation of our results, even including reflections (Extended Data Fig. 6a). Extended Data Fig. 6b reproduces the data and the modelled response discussed in Fig. 3 and compares them to the extracted charge-carrier density profile with photon reabsorption, considering ten reflections. Furthermore, a comparison of the extracted vertical charge-carrier profile with and without photon reabsorption is shown in Extended Data Fig. 6c for two representative pump delay times, where the negligible influence of photon reabsorption for the interpretation of our results becomes evident.

These simulations assume translational symmetry in the *x*-*y* plane and consider the effect of an emitter M located at (x_M, y_M, z_M) on the charge-carrier density $n(z,t)$ at position P ($x = 0, y = 0, z$) (Extended Data Fig. 6a). We integrate over all emitter positions inside the sample to retrieve the *e-h* pair density caused by photon reabsorption $n_\mathrm{pra}(z)$ as a function of depth *z* which is added to the total charge-carrier density $n(z,t)$ in each time step Δt. Without considering reflections at the interfaces of the sample, this leads to:

$$n_\mathrm{pra}(z) = \frac{\alpha^3}{8\pi} \int_0^L \mathrm{d}z_\mathrm{M}\, N_\mathrm{photon}(z_\mathrm{M}) \int_{-\infty}^{\infty} \mathrm{d}x_\mathrm{M} \int_{-\infty}^{\infty} \mathrm{d}y_\mathrm{M}\, \mathrm{e}^{-\alpha\sqrt{x_\mathrm{M}^2 + y_\mathrm{M}^2 + (z - z_\mathrm{M})^2}}$$

where $\frac{\alpha^3}{8\pi}$ is a normalization factor, $L = 500$ nm is the thickness of the sample and $\alpha = 0.238 \times 10^4$ cm^{-1} denotes the absorption coefficient at the wavelength of maximum photoluminescence measured on identical samples[36]. $N_{\mathrm{photon}}(z_{\mathrm{M}}) = k_2 n(z,t)^2 \Delta t$ is the number of photons reemitted at depth z_{M} in each time step. Analytically solving the integral along x_{M} and y_{M} yields:

$$n_{\mathrm{pra}}(z) = \frac{\alpha}{4}\int_0^L \mathrm{d}z_{\mathrm{M}} N_{\mathrm{photon}}(z_{\mathrm{M}}) \mathrm{e}^{-\alpha|z-z_{\mathrm{M}}|}(\alpha|z-z_{\mathrm{M}}|+1)$$

which is numerically integrated for each time step Δt. Finally, we consider reflections at the top and bottom interface of the sample by symbolically placing emitters outside the sample volume (Extended Data Fig. 6a), which is equivalent to backfolding the distribution beyond the sample boundaries into the sample. As an upper limit, we assume total reflection that is independent of the angle of incidence, leading to the following equation:

$$n_{\mathrm{pra}}(z) = \frac{\alpha}{4}\int_0^L \mathrm{d}z_{\mathrm{M}} N_{\mathrm{photon}}(z_{\mathrm{M}}) \left\{ \mathrm{e}^{-\alpha|z-z_{\mathrm{M}}|}(\alpha|z-z_{\mathrm{M}}|+1) + \sum_{\mathrm{i}=1}^{2}\sum_{\mathrm{k}=1}^{k_{\mathrm{R}}} \mathrm{e}^{-\alpha|z-z_{\mathrm{i,k}}|}\left(\alpha\left|z-z_{\mathrm{i,k}}\right|+1\right) \right\}$$

with

$$z_{1,\mathrm{k}} = (-1)^k \left(\left(2\left\lceil \frac{k+1}{2} \right\rceil - 2 \right) L + z_{\mathrm{M}} \right)$$

$$z_{2,\mathrm{k}} = (-1)^k \left(-2\left\lceil \frac{k}{2} \right\rceil L + z_{\mathrm{M}} \right).$$

Here k_{R} denotes the number of considered reflections and $\mathrm{i} = 1$ ($\mathrm{i} = 2$) is the term describing photons initially emitted towards the top (bottom) side of the sample.

Validation of the diffusion model. The validity of our approach can be verified by applying it to a high-resistivity silicon wafer as reference. Besides the 515-nm pump, we employ 1030-nm pump pulses, for which the absorption length in silicon (342 µm, ref. 59) is significantly larger than for excitation at 515 nm (2.6 µm, ref. 60). Extended Data Fig. 7a shows that the pump-induced waveforms for photoexcitation with 515 nm (green) display a clear shift to later EOS times t_{eos} with increasing pump delay time t_{p} (zero-crossings t_0 indicated by dashed lines), which is not present for excitation at 1030 nm (red). Following the same procedure as for $FA_{0.83}Cs_{0.17}Pb(I_{1-x}Cl_x)_3$, we extract the temporal positions of

639 the zero-crossings of the pump-induced waveforms as a function of t_p (Extended Data Fig. 7b) and apply
640 our model to extract the out-of-plane diffusion coefficient. In accordance with literature, we also
641 consider surface recombination. This allows us to accurately reproduce the measured zero-crossings
642 (modelled t_0 shown by dashed lines) for both excitation wavelengths with a diffusion coefficient of $D =$
643 $12\ \mathrm{cm^2 s^{-1}}$ and a surface recombination velocity of $S = 9 \times 10^4\ \mathrm{cm\ s^{-1}}$ in excellent agreement with
644 literature values[61,62]. The resulting charge-carrier density profiles for various pump delay times are
645 shown in Extended Data Fig. 7c. The difference between the two photoexcitation wavelengths is
646 obvious: For 515 nm, the steep initial carrier profile facilitates diffusion, leading to a rapid equilibration
647 of the density profile, resulting in strong shifts in the zero-crossing t0. For 1030 nm, the effect of
648 diffusion is strongly suppressed owing to the more homogeneous initial vertical carrier distribution and
649 the profile remains nearly identical within our time window, which manifests as a smaller change in the
650 temporal position of the zero-crossings.

Data availability

The data that support the plots within this paper are available from the publication server of the University of Regensburg at https://doi.org/10.5283/epub.58292.

References

43. Moon, K. et al. Quantitative coherent scattering spectra in apertureless terahertz pulse near-field microscopes. *Appl. Phys. Lett.* **101**, 011109 (2012).

44. Pronin, O. et al. High-power 200 fs Kerr-lens mode-locked Yb:YAG thin-disk oscillator. Opt. Lett. **36**, 4746–4748 (2011).

45. Cvitkovic, A., Ocelic, N. & Hillenbrand, R. Analytical model for quantitative prediction of material contrasts in scattering-type near-field optical microscopy. *Opt. Express* **15**, 8550 (2007).

46. Hauer, B., Engelhardt, A. P. & Taubner, T. Quasi-analytical model for scattering infrared near-field microscopy on layered systems. *Opt. Express* **20**, 13173 (2012).

47. Zhan, T. et al. Transfer matrix method for optics in graphene layers. *J. Phys.: Condens. Matter* **25**, 215301 (2013).

48. Liewald, C. et al. All-electronic terahertz nanoscopy. *Optica* **5**, 159–163 (2018).

49. Aghamiri, N. A. et al. Hyperspectral time-domain terahertz nano-imaging. *Opt. Express* **27**, 24231 (2019).

50. Davies, C. L., Patel, J. B., Xia, C. Q., Herz, L. M. & Johnston, M. B. Temperature-Dependent Refractive Index of Quartz at Terahertz Frequencies. *J. Infrared, Millimeter, Terahertz Waves* **39**, 1236–1248 (2018).

51. Frisenda, R. et al. Characterization of highly crystalline lead iodide nanosheets prepared by room-temperature solution processing. *Nanotechnology* **28**, 455703 (2017).

52. Mooshammer, F. et al. Quantitative terahertz emission nanoscopy with multiresonant near-field

probes. *Opt. Lett.* **46**, 3572 (2021).

53. Mester, L., Govyadinov, A. A. & Hillenbrand, R. High-fidelity nano-FTIR spectroscopy by on-pixel normalization of signal harmonics. *Nanophotonics* **11**, 377–390 (2022).

54. Hasselbeck, M. P. et al. Emission of terahertz radiation from coupled plasmon-phonon modes in InAs. *Phys. Rev. B* **65**, 233203 (2002).

55. Wang, S., Xiao, W. & Wang, F. Structural, electronic, and optical properties of cubic formamidinium lead iodide perovskite: a first-principles investigation. *RSC Adv.* **10**, 32364–32369 (2020).

56. Ndione, P. F., Li, Z. & Zhu, K. Effects of alloying on the optical properties of organic-inorganic lead halide perovskite thin films. *J. Mater. Chem. C* **4**, 7775–7782 (2016).

57. Poellmann, C. et al. Resonant internal quantum transitions and femtosecond radiative decay of excitons in monolayer WSe_2. *Nat. Mater.* **14**, 889-893 (2015).

58. Crothers, T. W. et al. Photon Reabsorption Masks Intrinsic Bimolecular Charge-Carrier Recombination in $CH_3NH_3PbI_3$ Perovskite. *Nano Lett.* **17**, 5782–5789 (2017).

59. Schinke, C. et al. Uncertainty analysis for the coefficient of band-to-band absorption of crystalline silicon. *AIP Adv.* **5**, 067168 (2015).

60. Vuye, G. et al. Temperature dependence of the dielectric function of silicon using in situ spectroscopic ellipsometry. *Thin Solid Films* **233**, 166–170 (1993).

61. Canali, C., Nava, F. & Reggiani, L. Drift Velocity and Diffusion Coefficients from Time-of-Flight Measurements. In *Hot electron transport in semiconductors*. *Topics in Applied Physics* vol. 58 87-112 (Springer Berlin Heidelberg, 1985).

62. Thomas, R. E. Silicon Solar Cells (2) – Practical Aspects. In *Solar Energy Conversion An Introductory Course*. First edition 805-830 (Pergamon Press, 1979).

63. Chen, Y. et al. Optoelectronic Properties of Mixed Iodide–Bromide Perovskites from First-Principles Computational Modeling and Experiment. *J. Phys. Chem. Lett.* **13**, 4184–4192

(2022).

64. Fu, M. et al. Unraveling exciton–phonon coupling in individual $FAPbI_3$ nanocrystals emitting near-infrared single photons. *Nat. Commun.* **9**, 3318 (2018).

65. Carpenella, V. et al. High-Pressure Behavior of δ-Phase of Formamidinium Lead Iodide by Optical Spectroscopies. *J. Phys. Chem. C* **127**, 2440–2447 (2023).

66. Julien, C., Mavi, H. S. & Chévy, A. Temperature Dependence of the Vibrational Properties of PbI_2. *Phys. Status Solidi* **177**, 143–155 (1993).

67. Pedesseau, L. et al. Vibrational properties of 2H-PbI_2 semiconductors studied via Density Functional Theory calculations. *Thin Solid Films* **541**, 9–11 (2013).